National-Scale Dynamic Water Resources Assessment Model in China

Huan Liu, Yangwen Jia, Jianhua Wang, Junkai Du, Cunwen Niu, Peng Hu, and Jiajia Liu

First edition published 2026

ISBN: 978-1-041-08697-0 (hbk)
ISBN: 978-1-041-08702-1 (pbk)
ISBN: 978-1-003-64664-8 (ebk)

Chapter 1

Model Architecture Design and Implementation Program of the CWAM

DOI: 10.1201/9781003646648-1

CRC Press
Taylor & Francis Group
Boca Raton London New York

CRC Press is an imprint of the
Taylor & Francis Group, an **informa** business

CHAPTER 1

Model Architecture Design and Implementation Program of the CWAM

1.1 IDENTIFICATION OF THE COMPLEXITY OF WATER YIELD MECHANISMS IN CHINA

1.1.1 Regional Heterogeneity in China

China is situated in the southeastern region of the Eurasian continent, bordered by the Pacific Ocean to the east. As of the end of 2023, China's total population was approximately 1.41 billion, with its GDP reaching 126,058 billion Yuan. The country covers 22,909 rivers with individual basin areas of over 100 km^2 and 2865 lakes with water surface areas of larger than 1 km^2, as illustrated in Figure 1.1. Geographically, China exhibits a step-like topography that descends from the high western regions to the lower eastern plains. China's topography is high in the west and low in the east, with a step-shaped distribution. The western part of the country is predominantly characterized by mountains and plateaus, while the eastern region is primarily composed of plains.

To facilitate comprehensive water resource management, China is further divided into 10 Class I water resources regions (WRRs), 80 Class II WRRs, and 210 Class III WRRs (Figure 1.2). The ten Class I WRRs include Songhuajiang River Basin (SRB), Liaohe River Basin (LRB), Haihe River Basin (HRB), Yellow River Basin (YRB), Huaihe River Basin (HURB), Yangtze River Basin (YZRB), Southeast River Basin (SERB), Pearl River Basin (PRB), Southwest River Basin (SWRB), and Northwest River Basin (NWRB).

The country encompasses an extensive territory that spans multiple climatic-hydrological zones and diverse geological and geomorphological units. This diversity leads to considerable spatial variability in water and thermal conditions, as well as geological features,

DOI: 10.1201/9781003646648-1

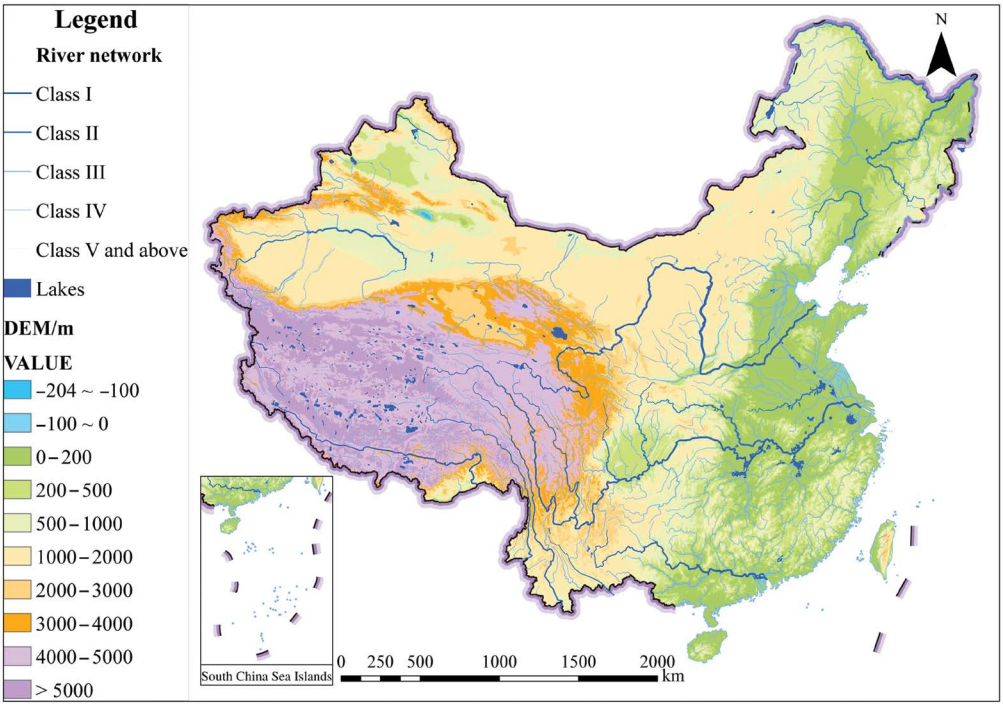

FIGURE 1.1 Topography and main rivers of China.

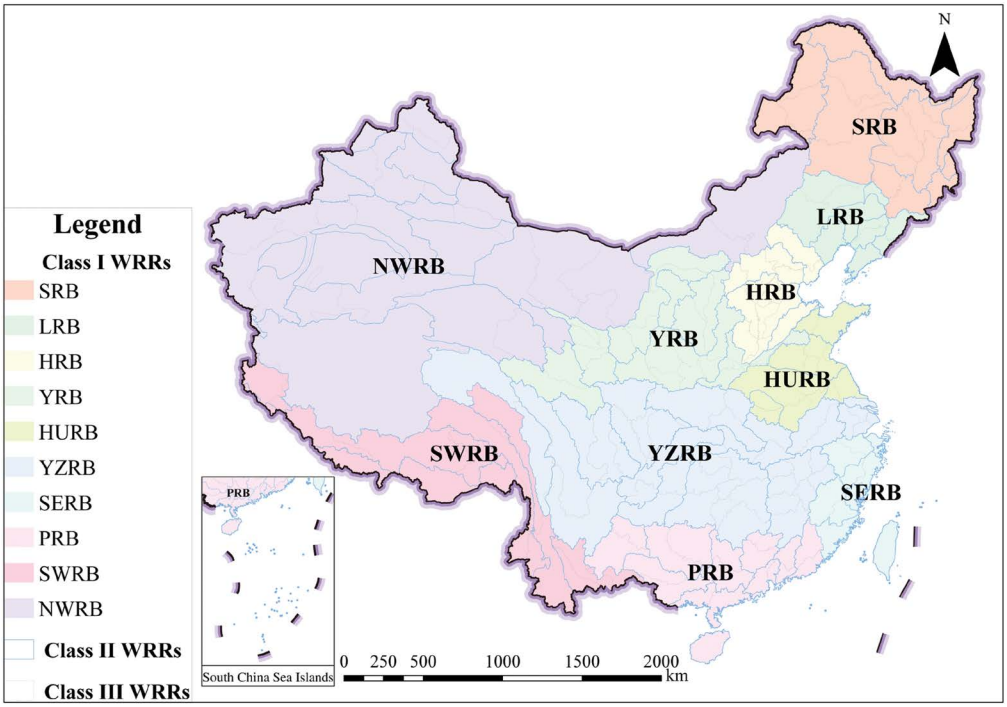

FIGURE 1.2 Water resources regions of China.

which traditional hydrological models for river basins fail to fully capture. Unlike a single river basin, China, as a large-scale region, exhibits the following characteristics.

1. It covers as many as ten climatic zones: Frigid Temperate Zone (FTZ), Median Temperate Zone (MTZ), Warm Temperate Zone (WTZ), Alpine Frigid Zone (AFZ), Alpine Subfrigid Zone (ASZ), Plateau Temperate Zone (PTZ), North Asian Tropical Zone (NATZ), Middle Asian Tropical Zone (MATZ), South Asian Tropical Zone (SATZ), and Marginal Tropical Zone (MTPZ). The water and thermal conditions vary greatly in different climatic zones. In the southern regions characterized by a humid climate, the saturation-excess runoff occurs regularly during rainfall events. Conversely, in the northern regions, the climate is dry, and the unsaturated zone of soil is thick, so infiltration-excess runoff is more common. In the case of semi-arid and semi-humid regions of the Huang-Huai-Hai River basin, both saturation-excess and infiltration-excess runoff exist. As a result, it is difficult to characterize the composite processes of saturation-excess and infiltration-excess runoff across the various climatic zones.

2. It has tens of thousands of rivers, each varying in shape, basin area, and network density. Moreover, China's northwest inland area occupies nearly one-third of the country, with many rivers flowing into inland lakes or disappearing into deserts. The surface flow model proposed by Jenson and Domingue (1988) is conventionally used to obtain the river networks and basins by setting a single sub-basin area threshold. Dealing with the complex river network structure of China, the method proposed by Jenson and Domingue (1988) exhibits certain limitations in accurately describing the boundaries of large-scale regions, determining outlets of the river basins, and identifying the rivers in inland regions.

3. It is a mountainous country, with approximately two-thirds of its landmass covered by mountains. Influenced by high topography change, the water and thermal conditions as well as vegetation show significant vertical zonal heterogeneity. Sevruk (1997) found that there exists a strong correlation between precipitation and elevation in large-scale mountainous regions. Furthermore, as elevation increases, vegetation type gradually changes from deciduous broadleaf forests to coniferous forests, then to alpine meadows, and ultimately to areas covered by glaciers and snow. This heterogeneity influences multiple model parameters, including leaf area index (LAI), fractional vegetation cover (FVC), canopy interception, and depression storage depth. Consequently, it is imperative to conduct a more precise examination of the vertical variations in model inputs and parameters.

4. It has a complex and diverse vadose zone structure that determines the redistribution of precipitation. Many rivers in China originate from highlands and mountainous regions where the soil is exposed to freezing temperatures (Li et al., 2008). The phase transition of water during freezing and thawing cycles significantly alters soil water potential, which affects the evapotranspiration and infiltration rates (Watanabe and

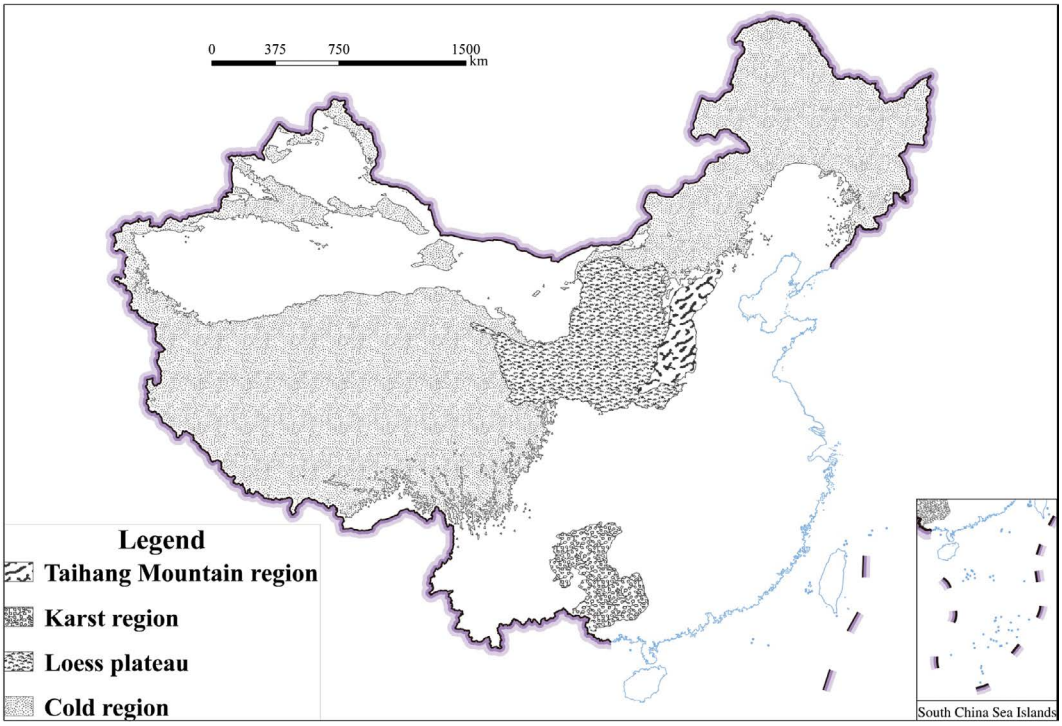

FIGURE 1.3 Schematic diagram of the distribution of the special vadose zone structures in China.

Osada, 2017). Simultaneously, one of the largest, continuous karst regions in the world is located in the Yunnan-Guizhou Plateau of southwest China (Zhang et al., 2011). Karst system has strong heterogeneity due to the existence of micropores, small fissures, and large fractures and conduits (Perrin et al., 2003; Hartmann et al., 2014). Moreover, swelling soils, as special soil types, are widely distributed all around the Loess Plateau in China. Swelling deformation occurs when swelling soils absorb water, affecting the distribution of soil pores and moisture movement (Su, 2010). Accurate description of the spatial heterogeneity of vadose zone structures is one of the important challenges to be solved. Figure 1.3 shows the spatial distribution of these special vadose zone structures in China. The karst region was determined with reference to the South China karst topographic map in National Natural Atlas of China. The Loess Plateau was from the Geographic Data Sharing Infrastructure at the College of Urban and Environmental Science, Peking University (http://geodata.pku.edu.cn). The cold region referred to Chen et al. (2005). It should be noted that Taihang Mountain Region is a typical soil-bedrock structure, which has been characterized in the WEP model.

1.1.2 Factors Affecting Water Yield in Large-Scale Regions

The water yield in large-scale regions under natural conditions is a complex and non-linear process, which is significantly influenced by climatic characteristics, subsurface conditions,

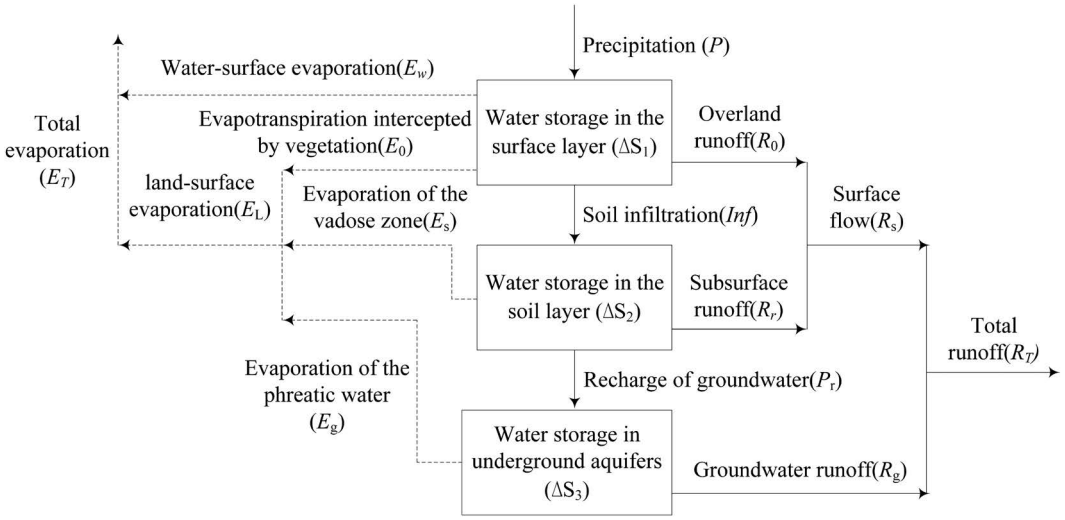

FIGURE 1.4 Schematic diagram of water yield processes.

and human activities. A schematic diagram illustrating the process of water yield in river basins is shown in Figure 1.4.

1.1.2.1 Climatic Conditions

Climate is the most basic and important factor affecting water yield in a river basin. It encompasses elements such as precipitation, air temperature, wind speed, relative humidity, and radiation. It is generally accepted that water yield is primarily governed by infiltration-excess runoff in river basins with a dry climate, while saturation-excess runoff predominates in river basins with a wet, perennial climate. Precipitation is the basic source of water resources in river basins and a key factor reflecting the wet and dry characteristics of the climate. The characteristics of precipitation directly affect infiltration and flow yield processes; meanwhile, air temperature, wind speed, relative humidity, and radiation affect soil moisture content and alter soil infiltration by controlling evapotranspiration within the river basin. For example, according to Wang et al. (2007), air temperature and evapotranspiration (*ET*) capacity in the YRB showed a good positive correlation, with an increase of 1°C in air temperature increasing the *ET* capacity by about 5.0%–7.0%. In addition, the structure of vadose zone becomes complicated with the change of air temperature. In the alpine zone, freezing of the soil occurs when the temperature drops, forming a permafrost layer, and thawing of the permafrost when the temperature rises. The alternation of soil freezing and thawing causes constant changes in effective soil water content, porosity, saturated hydraulic conductivity, etc., forming the special soil moisture dynamics in cold regions.

1.1.2.2 Subsurface Conditions

Among the various types of surface cover that influence the process of water yield in a river basin, geology, topography, vegetation type, and growth conditions play significant

roles. Geological conditions, including lithology, tectonics, the degree of joint development and weathering, and soil texture, influence precipitation infiltration, evapotranspiration, water storage, and the exchange between surface and groundwater runoff. Hard and dense rocks are unfavorable for precipitation infiltration, resulting in high runoff coefficients. Conversely, if the rocks are highly weathered or soluble, they enhance the hydraulic conductivity and water-holding capacity of vadose zone, resulting in abundant underground runoff, such as in karst areas. Surface soils can be broadly classified by texture into three types: sandy, clay, and loam. Of these, sandy soils have strong hydraulic conductivity and weak water-holding capacity, clay soils have poor hydraulic conductivity and strong water-holding capacity, and loamy soils have hydraulic conductivity and water-holding capacity somewhere in between. Topography, on the one hand, affects infiltration by influencing the intensity of rainfall water supply to the subsurface. When the intensity of rainfall is the same, the soil on flat surfaces receives more water than on sloping surfaces, and thus rainfall infiltration is more effective on flat surfaces. It was found that runoff coefficients were greater in steep topographic basins than in gently sloping basins for roughly the same climatic characteristics and air inclusion zone conditions (Rui, 1996). On the other hand, the steepness of the terrain due to gravity also affects the flow rate of runoff over the subsurface, altering the timing of production and the formation of runoff volumes. According to the simulation experiment of indoor artificial rainfall, the slope gradient is in the range of 20°; when the length of the flume is certain, the rate of water flow increases gradually with the increase in the slope. There was also a significant relationship between slope gradient and the amount of water yield (Zhang et al., 2008). Vegetation intercepts and redistributes precipitation through the canopy and litter layer, increasing infiltration and evapotranspiration, slowing runoff rates, and reducing runoff volume. Studies have shown that different types of vegetation differ in their ability to intercept and redistribute precipitation, with woodlands generally being larger than shrubs and shrubs larger than grasslands (Siriwardena et al., 2006). In addition, the better the vegetation growth condition (leaf area, vegetation cover, root depth, etc.), the greater the retention and storage of precipitation in general.

1.1.2.3 Human Activities

Human activities have significantly altered local climatic and subsurface conditions, affecting the process of water yield and the water-heat balance in both direct and indirect ways. Generally, the construction of hydraulic projects, such as reservoirs, dams, and transfer projects affect the natural transport of water and directly alter the quantity and spatial and temporal distribution characteristics of natural river runoff. The construction of residential and industrial areas has resulted in hardened surfaces and a substantial increase in the percentage of impervious areas (IAs) in river basins. This change hinders the infiltration of precipitation while reducing the surface's ability to retain and store water. This resulted in a significant increase in flood flow, a shortening of the peak occurrence time, and a significant increase in the runoff coefficient. Agricultural development and soil and water conservation change soil geological conditions and local topography, thereby affecting the time-range distribution processes of precipitation and evapotranspiration.

Furthermore, the over-exploitation of water resources results in a continuous decline in groundwater levels and an increase in the thickness of vadose zones, leading to a decrease in the surface runoff coefficient and altering the interrelationship between surface water and groundwater.

1.1.3 Spatial Heterogeneity Characteristics of Water Yield Mechanisms

China has a vast area, diverse climate types, and complex subsurface conditions, which have led to significant regional differences in water production mechanisms. These variations can be summarized in the following four aspects:

1.1.3.1 Coexistence of Saturation-Excess and Infiltration-Excess Runoff

In humid climatic areas, the vadose zone can easily become saturated following rainfall, resulting in saturation-excess runoff. Conversely, in areas with a dry climate and a high thickness of the vadose zone, vegetation conditions are poor, and the precipitation is low, primarily occurring as heavy rainfall. For these areas, it is difficult for the vadose zone to become saturated by small amounts of precipitation. Therefore, the primary cause of runoff is that the intensity of rainfall exceeds the infiltration capacity of the surface soil. Of course, some arid areas may be distributed with meadows, swamps, or be recharged by snowmelt and ice melt, resulting in high soil moisture in these areas, which is easily saturated. In addition, in semi-arid and semi-humid areas, saturation-excess and infiltration-excess runoff can occur simultaneously. With changes in precipitation characteristics, soil moisture content, etc., the form of runoff yield in these areas undergoes a rapid transformation, and the precipitation-runoff relationship becomes more complex.

1.1.3.2 Coexistence of Water Yield in Cold and Non-Cold Regions

Glaciers, snow, and permafrost cause water yield mechanisms in cold regions that differ significantly from those in non-cold regions. As temperatures rise in the spring, glaciers, snow, and permafrost in cold regions thaw to recharge river runoff, which is the main reason why spring flooding occurs in many rivers. In addition, the freezing and thawing of soils in vadose zones with temperature changes creates special soil moisture dynamics in cold regions, which profoundly affects and alters the mechanism of water yield in cold regions. When the soil freezes as the temperature drops, the soil pores are closed, making it difficult for water to infiltrate. As temperatures rise and permafrost thaws, the soil's capacity to infiltrate and store water increases, and the interaction between surface water and groundwater becomes active. The rainfall-runoff coefficient for permafrost can reach up to 0.7, which is significantly higher than that of non-permafrost areas.

1.1.3.3 Coexistence of Water Yield in Mountainous Areas and Plains

The process of water yield in mountainous areas is affected by changes in elevation, in contrast to the horizontal variability observed in plains areas. In alpine areas where the terrain is highly undulating, water and heat conditions, vegetation types, and growth are characterized by vertical variations. Sevruk et al. (1997) pointed out that in large and mesoscale mountains, precipitation is influenced by topographic elements such as elevation, slope of

the subsurface, and slope direction. Among these factors, the relationship between precipitation and elevation is the closest. As altitude increases, the vegetation type transitions from deciduous broadleaf forests to coniferous forests, then to alpine meadows, and finally to glacial snow cover, resulting in vertical changes in vegetation parameters such as LAI and vegetation cover. Consequently, there are large differences in the hydrothermal state and vegetation characteristics of different elevation zones, which directly affect the process of water yield such as evapotranspiration and infiltration.

1.1.3.4 Coexistence of Water Yield in Soil and Rock Structure

There are significant differences in the lithology, thickness, and structure of vadose zones that affect the process of water yield. For mountainous areas composed of soluble rocks, such as carbonate rocks, the karst development within vadose zones is strong, resulting in the formation of numerous caverns, dissolution fissures, and lysimetric holes, which makes the recharge and discharge of groundwater very rapid. For non-karst mountainous areas, the bedrock of vadose zones generally has rock-forming fissures, tectonic fissures, and weathering fissures. Influenced by the depth, size, number, and connectivity of rift development, the structure of vadose zones has strong spatial heterogeneity. In addition, in loess areas, there exists a special structure such as large pores and vertical joints, where the soil swells with water absorption and shrinks with water loss, thereby affecting the distribution of soil pores and the process of water movement. The vadose zones and aquifers in the plains consist of huge thicknesses of loose Quaternary sediments with good water storage conditions. Groundwater recharge is mainly based on precipitation infiltration.

1.2 FUNCTION POSITIONING AND SELECTION OF THE CHINA WATER ASSESSMENT MODEL (CWAM)

1.2.1 Model Functional Requirements

The large-scale region has a vast area and distinctive features and is subject to the combined influence of various climates, topographies, vegetation, and the structure of vadose zones. The mechanisms governing water yield exhibit both diversity and complexity. However, traditional distributed hydrological models for river basins are mostly for complete basins and are limited to the extent of the study area and the types of climate and subsurface conditions they can cover. Consequently, the traditional hydrological model is not sufficient for national-scale water resources assessment in four main aspects of model construction: calculation unit division, model input, spatial parameterization, and simulation methods.

In order to achieve a refined simulation of hydrological processes and a dynamic assessment of water resources in the country, the model should possess the following functions:

1. It is capable of efficiently and rapidly dividing computation units and encoding their topological relationships for multiple river basins with independent catchment relationships in a large-scale region. This ensures that the water balance and the paths of converging water flows within the computation units are not distorted during large-capacity simulations.

2. It is able to realize the coupled simulation of hydrothermal processes to adapt to the complex water and energy conditions present under the diverse climatic characteristics nationwide. Water cycle and heat cycle processes interact and are closely related, especially in cold regions.

3. It is capable of simultaneously portraying both saturation-excess and infiltration-excess runoff, to reflect the complex characteristics of water yield under varying climatic and geological conditions in this country. Due to the spatial and temporal variability of rainfall and the structural diversity of vadose zones, coupled with the impact of human activities, the water yield mechanism is quite complex, involving a variety of forms, such as hyper-permeable surface runoff, saturated surface runoff, runoff in the soil, and groundwater runoff.

4. It is able to make full use of the existing multi-source data to complete the model inputs and the effective assignment of parameters on the computation units to reflect the spatial and temporal variability of meteorological, hydrological, soil, vegetation, and other information on a nationwide scale. Model inputs and parameters are critical in determining the accuracy of model simulations. However, they vary significantly with climate characteristics and physical geographic conditions, affecting the hydrological response of the river basin.

5. It is capable of simulating hydrological processes such as evapotranspiration, evaporation, snowmelt, infiltration and soil water movement, groundwater movement and its exchange with rivers, and slope and river confluence based on the principle of balance of water, energy, and momentum, in order to support the quantitative analysis of hydrological variables, water resources, and their spatial and temporal evolution.

1.2.2 Investigation and Selection of Large-Scale Hydrological Models

Hydrological models, especially distributed physical hydrological models, are seen as a product of the combination of water yield and confluence theory and computer technology. Wagener et al. (2004) argued that any hydrological model can be expressed as equation (1.1):

$$Q = M_L(\theta_L / I) + \varepsilon_L \tag{1.1}$$

where Q is the simulated flow at the river basin outlet; M_L and θ_L are the model structure and parameters, respectively; I is the model input; and ε_L is the local error.

It can be seen that the construction of a hydrological model is to determine a reasonable set of model structure and parameters to provide a scientific description of the natural geographic conditions of a particular catchment/region and its corresponding processes of water yield and confluence. Therefore, a model with appropriate parameters and structure needs to be selected as the basis for the design and development of a distributed hydrothermal coupling model for large-scale regions. Based on the existing studies, nine (semi-) distributed hydrological models that are currently more widely used at home and abroad were investigated. Among them, the models developed by foreign scholars include TOPMODEL

(Kirkby and Beven, 1979), SHE (Abbott et al., 1986a; Abbott et al., 1986b), IHDM (Calver, 1988), TOPKAPI (Ciarapica and Todini, 2002), VIC (Liang et al., 1994), and SWAT (Arnold and Fohrer, 2005); the models developed by Chinese scholars include DTVGM (Xia et al., 2004), GBHM (Wang et al., 2006), and WEP-L (Jia et al., 2006). These models are analyzed in terms of computation unit divisions, water yield mechanisms, confluence calculations, structural characteristics, and scope of application, as listed in Table 1.1.

TABLE 1.1 Comparison of Commonly Used Semi-distributed and Distributed Hydrological Models

Hydrological Models	Computation Unit Divisions	Water Yield Mechanisms	Confluence Calculations	Structural Characteristics	Scope of Application
TOPMODEL	Grids/sub-basins	Saturation-excess runoff	Slope runoff hysteresis function and channel evolution function	Based on topography and variable flow area theory; effects of precipitation, evaporation, etc. not considered	Used in uninformative areas, suitable for river basins with high topographic relief
SHE	Grids	One-dimensional Richards equation	Continuity and momentum equations in the St. Venant equations	Outstanding physical mechanism; complex structure and cumbersome calculations	Soil slopes, but difficult to apply to large-scale river basins
IHDM	Geomorphological unit	Two-dimensional Richards equation	One-dimensional wave equation of motion	River basin is divided into a number of drop channels and representative slopes	Suitable for simulation of storm flow in small catchments
TOPKAPI	Grids	Saturation-excess runoff	Wave equation of motion	The model parameters are strongly influenced by the grid scale, and the water movement is described by three "structurally similar" non-linear equations.	The scale is in the tens to thousands of square kilometers
VIC	Grids	Saturation-excess and infiltration-excess runoff	Instantaneous unit line method, Brooks - Corey formula, Arno model	Soil water storage capacity area distribution curve; infiltration capacity area distribution curve	Large-scale regions
SWAT	Sub-basins	CSC curve method, Green-Ampt model, Manning's formula	Muskingum method	Not suitable for detailed modeling of single flood processes	Water quality and quantity modeling in river basins at different scales
DTVGM	Grids/sub-basins	Water balance	Wave equation of motion	Integrating Hydrological Systems Theory with Distributed Modeling	River basins with a lack of hydrological information
GBHM	Geomorphological unit	One-dimensional Richards equation	One-dimensional wave equation of motion	Discrete method using unit lines combined with terrain properties	Small- or medium-scale catchment
WEP-L	Contour belts	Theory of various source areas	One-dimensional wave equation of motion	Coupled simulation of water and energy exchange processes, reflecting the theory of variable water area	Large-scale river basin

Different hydrological models have unique characteristics due to the different modeling objectives, ideas, and structures. Considering the spatial variability of water yield mechanisms nationwide, we choose to design and develop the CWAM based on the WEP-L model. The reason for this is that the WEP-L model structure has advantages in water resources assessment in large-scale river basins and has been successfully applied in the YRB and other areas.

1.2.3 WEP-L Model and Dynamic Water Resources Assessment

The water and energy transfer processes (WEP) model (Jia et al., 2001) was developed by combining the merits of physically based spatially distributed (PBSD) hydrological models and soil vegetation atmosphere transfer (SVAT) models. The model has been successfully applied in several river basins in Japan, Korea, and China with different climate and geographic conditions (Jia and Tamai, 1998; Jia et al., 2001, 2002, 2005). The WEP model has the following main characteristics: (1) combined modeling of hydrological processes and energy transfer processes, (2) consideration of the land use heterogeneity inside a computation unit by adopting the mosaic method (Avissar and Pielke, 1989), and (3) incorporation of the runoff generation theory of various source areas (Hewlett, 1982) into the model through a numerical simulation in groundwater/subsurface water flow to directly reflect topography's effects in runoff generation, thus capable of modeling infiltration excess, saturation excess, and mixed runoff generation mechanism.

To make the WEP model applicable for water resources assessment in large river basins like the YRB, the following main improvements were performed and the WEP-L model was established consequently: (i) instead of grid cells, contour belts inside small sub-basins, which were obtained based on a digital elevation model (DEM) of 1-km resolution and the area of every sub-basin less than 100 km^2, were used as computation units, and the Pfafstetter coding rule (Verdin and Verdin, 1999) was adopted to code subdivided river links and sub-basins to aid hydrological modeling in the large river basin; (ii) the soil-vegetation (SV) land use group in the WEP model was further divided into three groups of SV (grassland, forest, and bare soil land), irrigated farmland (IF), and non-irrigated farmland (NF) to consider cultivation and irrigation effects on hydrological processes; (iii) a water allocation and regulation method was developed and then coupled to WEP-L to model water use processes like reservoir regulation, canal diversion and water allocation in a coupling way with natural hydrological processes; (iv) spatial and temporal interpolations of social-economy and water use data were carried out; and (v) a snow melt model based on the temperature-index approach was developed to reflect the impacts of snow storage and melting on hydrological and energy processes as well as water resources.

1.3 MODEL ARCHITECTURE DESIGN OF THE CWAM

1.3.1 Model Framework

Based on the WEP-L model, the construction of the CWAM was divided into four major parts: determination of basic computation units, model inputs, spatial parameterization, simulation of water/energy cycle processes, and outputs. Furthermore, each part of the

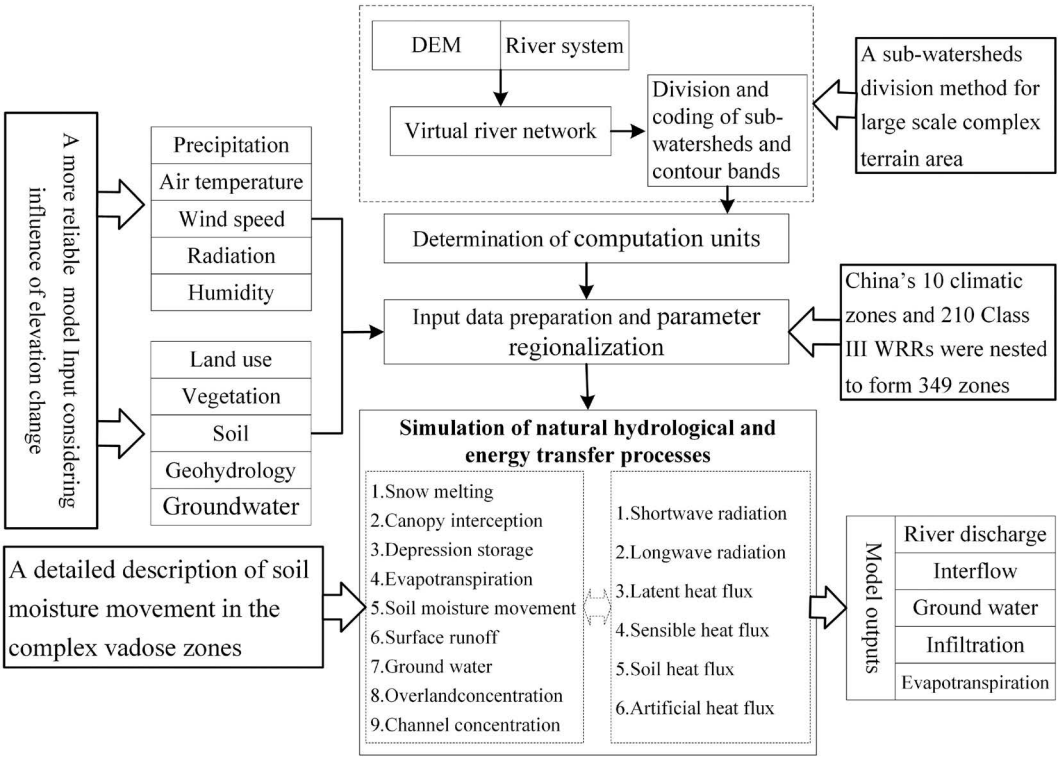

FIGURE 1.5 Schematic illustration of the architecture of the CWAM.

WEP-L model was improved to address the deficiencies in the refined simulation of large-scale hydrological processes, as shown in Figure 1.5.

1. A sub-basin division method was proposed based on automatic recognition of river basin outlets and fusion of river network with variable sub-basin area thresholds. The method mainly included the determination of river basin outlets as well as the maximum and minimum area thresholds of sub-basins, multi-threshold virtual river network integration, and sub-basin division and codification. It considered both computation efficiency and accuracy of sub-basin division, which provides an efficient basis for developing a distributed hydrological model in large-scale regions. The related study has been published in Advanced Engineering Sciences (Liu et al., 2019). Details were set out in Chapter 2.

2. Meteorological data, such as precipitation and air temperature, and vegetation data, such as LAI and coverage, are key inputs to hydrological models. Such data are significantly affected by topographic relief. Based on China's 80 Class II WRRs, the regression relationships between precipitation and air temperature with elevation were established in each WRR. Furthermore, instead of the original plane interpolation method, a three-dimensional interpolation method considering elevation effects was adopted to interpolate precipitation and air temperature. Vegetation data of different

elevation zones were obtained using the remote sensing/geographic information system (RS/GIS) techniques. Details were set out in Chapter 2.

3. The vadose zone was simply characterized as a soil-bedrock structure in the WEP model, where soil moisture movement parameters were only determined based exclusively on the texture information of different soil types (Jia et al., 2006). However, these parameters failed to reflect the soil moisture dynamics of the special vadose structure in the karst region, Loess Plateau, and cold region. Therefore, before the development of the CWAM, we carried out experimental observations and modeling of the infiltration-produced flow processes under these special conditions to better understand these phenomena. Details were set out in Chapters 3–5, respectively. To take into account the simulation efficiency of the CWAM, we focused on the soil moisture movement in the special vadose zones on the large-scale regions and simplified the simulation process of the previous small-scale regions. The effects of soil swelling deformation, karst development, and soil freezing-thawing on soil moisture movement were quantitatively analyzed, and the related parameters were modified.

4. Regarding the calibration and validation of the national model, it is very important to achieve efficient parameter regionalization. There are three categories and dozens of parameters in the WEP model, and the methods for evaluating initial values of parameters have been described in detail by Jia et al. (2006). Furthermore, considering spatial heterogeneity of meteorological hydrology and underlying surface conditions, China's 10 climatic zones and 210 Class III WRRs were nested to form 349 zones. These zones were used as the parameter tuning units in the CWAM. Details were set out in Chapter 6. Based on the verified CWAM, we have carried out a systematic analysis of water resources and their spatial variability across the country and its different climatic and geomorphic regions. Details were set out in Chapters 7 and 8.

1.3.2 Basic Structure and Modeling Approaches for Main Processes of the WEP-L Model

1.3.2.1 Model Basic Structure

The vertical structure of WEP-L within a contour belt was shown in Figure 1.6, and the horizontal structure within a sub-basin was shown in Figure 1.7. Land use was divided into five groups within a contour belt, namely, SV group, NF group, IF group, water body (WB) group, and IA group. The SV group was further classified into bare soil land, tall vegetation (forest or urban trees), and short vegetation (grassland). The IA group included impervious urban cover, urban canopy, and rocky mountains. The areal average of water and heat fluxes from all land uses in a contour belt produced the averaged fluxes in the contour belt. For pervious groups of SV, NF, and IF, nine vertical layers, namely, an interception layer, a depression layer, three upper soil layers, a transition layer, an unconfined aquifer, an aquitard, and a confined aquifer, were included in the model structure.

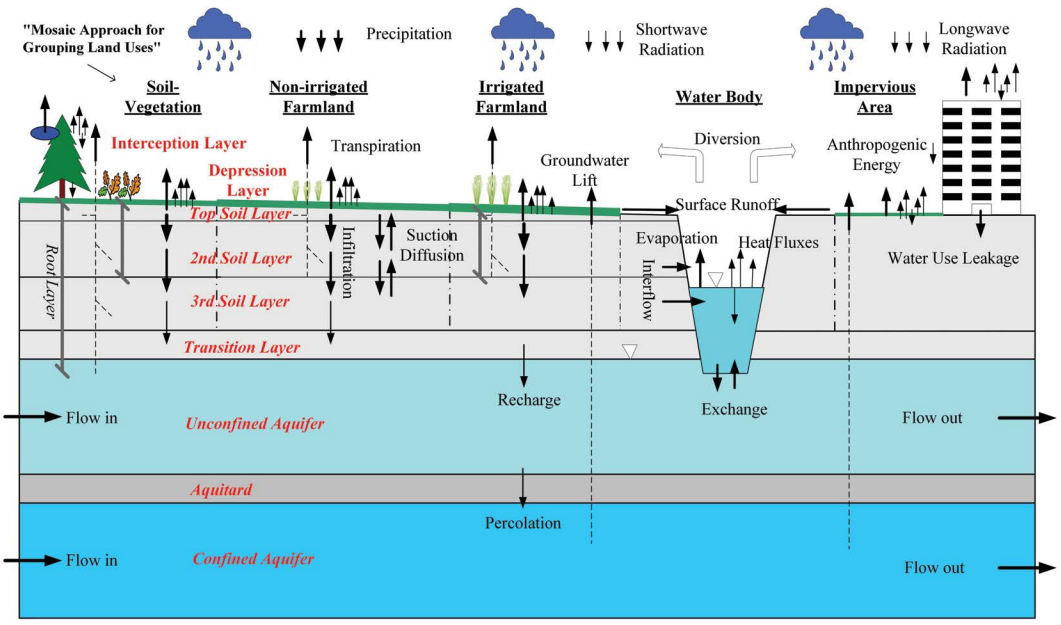

FIGURE 1.6 Vertical structure within a contour belt of the CWAM.

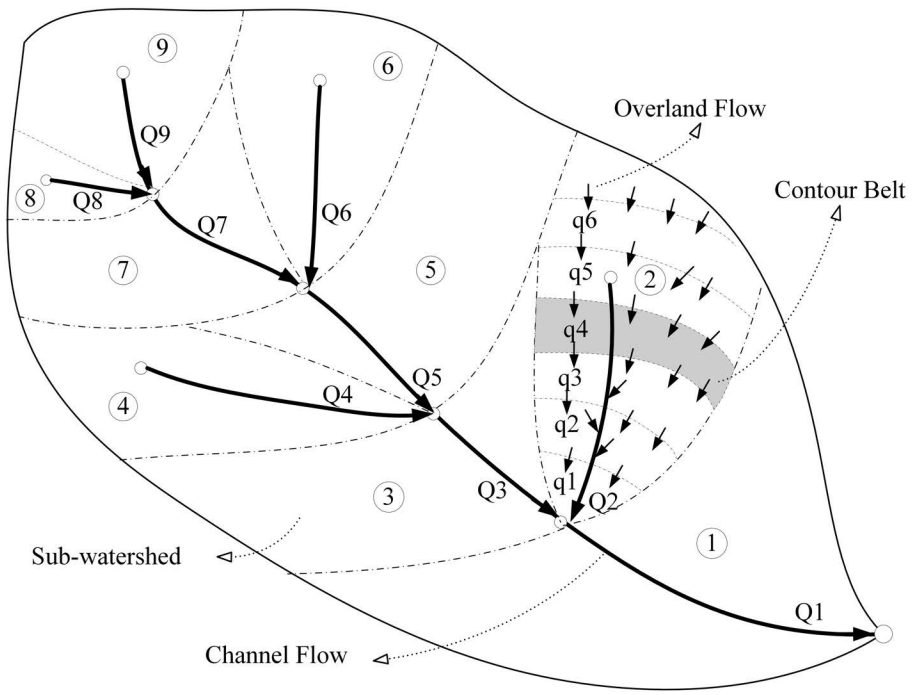

FIGURE 1.7 Horizontal structure within a sub-basin of the CWAM.

1.3.2.2 Model Calculation Methods

(1) Calculation of Energy Processes The energy cycle directly affects and constrains water cycle processes such as evapotranspiration, snowmelt, and soil freezing and thawing in the river basin, as shown in Figure 1.8. The energy balance formulas include equations (1.2) and (1.3):

$$RN + A_e = LE + H + G + P_L + A_d \tag{1.2}$$

$$RN = RS - \alpha RS + RLD - RLU \tag{1.3}$$

where RN is the net radiation; LE is the latent heat flux; H is the sensible heat flux; G is the heat transfer in the ground; A_e is the artificial radiation; PL is the plant uptake (about 2% of the RN); A_d is the shifting term (which is often neglected except for oases and lakes); RS is the shortwave radiation reaching the surface; RLD and RLU are the atmosphere-to-surface and surface-to-atmosphere longwave radiation, respectively; α is the shortwave emissivity; the units of radiation and heat flux are MJ/m^2; and α is the shortwave emissivity; the units of radiation and heat flux are MJ/m^2.

The simulated energy transfer processes included short-wave radiation, long-wave radiation, latent heat flux, sensible heat flux, and soil heat flux.

The formulas for calculating daily short-wave radiation include equations (1.4)–(1.9):

$$RS = RS_0\left(a_s + b_s\frac{n}{N}\right) \tag{1.4}$$

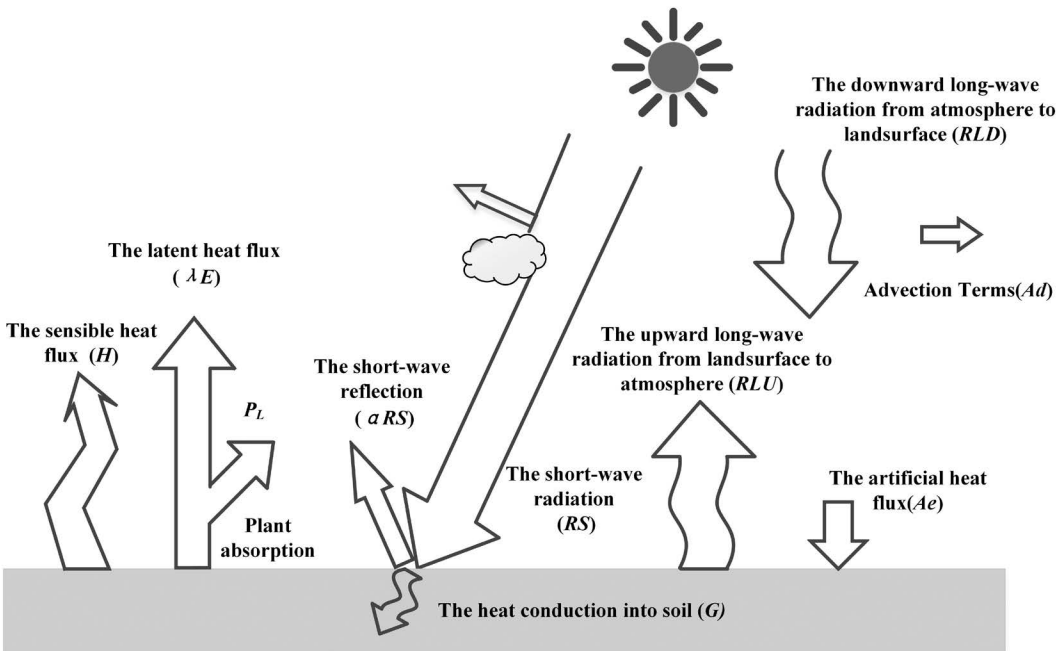

FIGURE 1.8 Schematic of land-atmosphere energy exchange.

$$RS_0 = 38.5 d_r (\omega_s \sin\phi \sin\delta + \cos\phi \cos\delta \sin\omega_s) \tag{1.5}$$

$$d_r = 1 + 0.33 \cos\left(\frac{2\pi}{365} J\right) \tag{1.6}$$

$$\omega_s = \arccos(-\tan\phi \tan\delta) \tag{1.7}$$

$$\delta = 0.4093 \sin\left(\frac{2\pi}{365} J - 1.405\right) \tag{1.8}$$

$$N = \frac{24}{\pi} \omega_s \tag{1.9}$$

where RS_0 is the short-wave radiation outside the atmosphere, and the unit of daily radiation and heat flux is MJ/m^2/day if not specified; as is the short-wave radiation diffusion constant (generally 0.25); b_s is the direct short-wave radiation constant (generally 0.5); n is the number of hours of sunshine; N is the number of hours of possible sunshine; d_r is the relative distance between the sun and the earth; w_s is the solar time angle at sunset; φ is the dimension of the observation point (positive in the northern hemisphere and negative in the southern hemisphere); δ is the solar inclination; J is the number of Julian days (from 1 January of each year); and the rest of the parameters have the same significance as above.

The formulas for calculating daily long-wave radiation include equations (1.10)–(1.12):

$$RLN = RLD - RLU = -f\varepsilon\sigma(T_a + 273.2)^4 \tag{1.10}$$

$$f = a_L + b_L \frac{n}{N} \tag{1.11}$$

$$\varepsilon = -0.02 + 0.261 \exp(-7.77 \times 10^{-4} T_a^{\,2}) \tag{1.12}$$

where f is the cloud impact factor; ε is the net emissivity; σ is the Stefan-Boltzmann constant (taking the value of 4.903×10^{-9} MJ m^{-2} K^{-4} day^{-1}); T_a is the average daily air temperature (°C); a_L is the constant of the long-wave emissivity (0.1 in arid regions, and 0.3 in humid regions); b_L is the constant of the long-wave emissivity (0.9 in arid regions, and 0.7 in humid regions); the rest of the parameters have the same meaning as above.

The formulas for calculating latent heat include equations (1.13) and (1.14):

$$LE = L \times E \tag{1.13}$$

$$L = 2.501 - 0.002361 T_s \tag{1.14}$$

where L is the latent heat of water (MJ/kg); T_s is the ground surface temperature (°C); and E is evapotranspiration (mm).

The formula for calculating sensible heat is expressed as equation (1.15):

$$H = \frac{\rho_a C_P (T_s - T_a)}{r_a} \tag{1.15}$$

where ρ_a is the air density (kg/m^3); C_P is the constant pressure specific heat of air (J/kg/°C); r_a is the aerodynamic impedance (s/m); the rest of the parameters have the same meaning as above.

The formula for calculating heat conduction into soil is expressed as equation (1.16):

$$G = \frac{c_s d_s (T_2 - T_1)}{\Delta t} \tag{1.16}$$

where G is the heat conduction into soil (MJ/kg); d_s is the thickness of the affected soil layer (m); T_1 and T_2 are the surface temperature (°C) at the beginning and end of the period, respectively; k_s is the soil heat transfer coefficient (Wm^{-1} K^{-1}); and c_s is the soil heat capacity coefficient (MJ m^{-1} K^{-1}).

Furthermore, the force-restore method (FRM) was used to solve the surface temperature of different land covers. This method is a better approximation to the classical heat diffusion equation compared with other methods. Hu and Islam (1995) suggested an optimal parameter α, which cannot only ensure minimum distortion of FRM to sinusoidal diurnal forcing but also make the distortion to higher harmonics negligible. They are followed in this research with equations (1.17)–(1.20):

$$\alpha \frac{\partial T_s}{\partial t} = \frac{2}{c_h \cdot d_0} G - w(T_s - T_d) \tag{1.17}$$

$$\frac{\partial T_d}{\partial t} = \frac{1}{\tau}(T_s - T_d) \tag{1.18}$$

$$\alpha = 1 + 0.943\left(\frac{\delta}{d_0}\right) + 0.233\left(\frac{\delta}{d_0}\right)^2 + 0.0168\left(\frac{\delta}{d_0}\right)^3 - 0.00527\left(\frac{\delta}{d_0}\right)^4 \tag{1.19}$$

$$d_0 = \sqrt{2k_h/(c_h w)} \tag{1.20}$$

where G is the heat conduction into soil; T_s is the surface temperature; T_d is the deep soil temperature (approximated as the daily average of T_s), υ is the considered soil depth (selected as the thickness of top soil layer); d_0 is the damping depth of the diurnal temperature wave, k_h is the soil heat conductivity, c_h is the soil volumetric heat capacity; $\omega = 2\pi/\tau$ and $\tau = 86400$. The soil thermal properties depend on the water content and the mineral composition of the soil.

(2) Calculation of Hydrological Processes The simulated hydrological processes included snow melting, evapotranspiration, infiltration, surface runoff, subsurface runoff, groundwater flow, overland flow, and river flow.

① *Evapotranspiration* Evapotranspiration in a contour belt consists of interception of vegetation canopies (evaporation from the wet part of leaves), evaporation from WB, soil, urban cover, and urban canopy, and transpiration from the dry fraction of leaves, with the

source from the three upper soil layers. The averaged evapotranspiration E is expressed as equation (1.21):

$$E = F_w E_w + F_{sv} E_{sv} + F_U E_U \tag{1.21}$$

where, F_W, F_{SV}, and F_U are the area fractions of WB, SV, and IA, respectively; E_W, E_{SV}, and E_U are the evaporation or evapotranspiration from them, respectively.

The evaporation from the WB or the ponded water in the depression storage was calculated using the Penman equation (1.22):

$$E_w = \frac{(RN - G)\Delta + \rho_a C_p \delta_e / r_a}{\lambda(\Delta + \gamma)} \tag{1.22}$$

where RN is the net radiation; G is the heat conduction into the soil; Δ is the gradient of saturated vapor pressure to temperature; δ_e is the air vapor pressure deficit, r_a is the aerodynamic resistance, ρ_a is the air density; C_p is the air specific heat; λ is the latent heat of the water and the psychometric constant.

The evaporation from the IA was taken as the smaller one of current depression storage and the potential evaporation. In this study, the maximum depression storage of IA is assumed as 5 mm.

The evapotranspiration from the SV group is calculated as equation (1.23):

$$E_{sv} = E_{i1} + E_{i2} + E_{tr1} + E_{tr2} + E_s \tag{1.23}$$

where E_i is the interception of vegetation; E_{tr} is the transpiration from the dry part of vegetation leaves, with numbers 1 and 2 representing tall vegetation and short vegetation, respectively, and E_s is the evaporation from soils.

The computation of interception is referred to the Noilhan and Planton (1989) model, which is an interception reservoir method. The evaporation from soil is assumed to come only from the topsoil layer. The formulas include equations (1.24)–(1.28):

$$E_i = Veg \cdot \delta \cdot E_v \tag{1.24}$$

$$\partial W_r / \partial t = Veg \cdot \delta \cdot E_v \tag{1.25}$$

$$R_r = \begin{cases} 0 & W_r \le W_{r\max} \\ W_r - W_{r\max} & W_r > W_{r\max} \end{cases} \tag{1.26}$$

$$\delta = (W_r - W_{r\max})^{2/3} \tag{1.27}$$

$$W_{r\max} = 0.2 \cdot Veg \cdot LAI \tag{1.28}$$

where Veg is the fraction of tall (or short) vegetation in the SV group; δ is the fraction coefficient of the foliage covered by a water film; E_v is the potential evaporation on vegetation

surface; W_r is the storage of the interception reservoir; W_{rmax} is the maximum W_r; P is the precipitation; R_r is the drainage rate from the canopy when W_r exceeds W_{rmax} and LAI is the leaf area index.

The actual transpiration was calculated using the Penman–Monteith equation (Monteith, 1973) and the canopy resistance (Noilhan and Planton, 1989), which is related to the soil moisture condition. The formulas include equations (1.29) and (1.30):

$$E_{tr} = Veg \cdot (1-\delta) \cdot E_{PM} \tag{1.29}$$

$$E_{PM} = \frac{(RN-G)\Delta + \rho_a C_p \delta_e / r_a}{\lambda[\Delta + \gamma(1 + r_c / r_a)]} \tag{1.30}$$

where E_{PM} is the Penman–Monteith transpiration; r_c is the canopy resistance, and the others as denoted above.

The transpiration is supplied from the soil layers by the roots. A root uptake model is adopted, which assumes that the root uptake intensity linearly decreases with the increase of root depth, and the uptake in the upper half root zone accounts for 70% of the total uptake. The transpiration of tall vegetation is assumed to originate from the three upper soil layers in Figure 1.6, while that of short vegetation originates from only the two upper ones.

The aerodynamic resistance r_a under neutral atmospheric conditions can be represented as equation (1.31) (Monteith, 1973):

$$r_a = \frac{\ln[(z-d)/z_{om}] \cdot \ln[(z-d)/z_{ox}]}{\kappa^2 U} \tag{1.31}$$

where z is the measurement height of wind speed, humidity, and temperature; κ is the von Karman constant; U is the wind speed; d is the displacement height; z_{om} is the roughness height of momentum, and $z_{ox} = z_{om}$ for momentum transfer, z_{ov} (the roughness height of vapor) for vapor transfer or z_{oh} (the roughness height of heat) for heat transfer, respectively. The Monin–Obukhov similarity theory is used to modify the computation of aerodynamic resistance (Brutsaert, 1982) under unstable and stable atmospheric conditions.

The canopy resistance r_c is also called the surface resistance. Noilhan and Planton (1989) are followed to calculate it. It is a summation of the contributions of the stomatal resistance of individual leaves. The formula can be expressed as equation (1.32):

$$r_c = \frac{r_{s\min}}{LAI} f_1(T) f_2(VPD) f_3(PAR) f_4(\theta) \tag{1.32}$$

where r_{smin} is the canopy minimum stomatal resistance; LAI is the canopy leaf area index; f_1 is the dependence on the air temperature T, f_2 is the dependence on the vapor pressure deficit (VPD) of the air; f_3 is the influence of the photosynthetically active radiation flux (PAR); f_4 is the effect of the soil moisture content.

Evaporation from soils was assumed to come only from the top layer. It was usually estimated by multiplying the potential evaporation (based on the Penman equation) by an evaporation coefficient, which is called the potential method hereafter. However, the

potential method may cause theoretical nonconsistency of heat flux partition on the soil surface because the net radiation and soil heat flux corresponding to the saturated vapor pressure of soil are used in the Penman equation, while the actual soil may be unsaturated. Based on the energy balance on the soil surface, aerodynamic diffusion equations of latent and sensible heat fluxes, and the wetness function concept, we derived the modified Penman equation (1.33) to compute actual soil evaporation directly.

$$E_s = \frac{(RN - G)\Delta + \rho_a C_p \delta_e / r_a}{\lambda[\Delta + \gamma(1 + \gamma/\beta)]} \tag{1.33}$$

where β is the wetness function, and the other notations are the same as mentioned above.

The wetness function is defined as in equation (1.34) (Lee and Pielke, 1992) and it is estimated by equation (1.35), which is a modified version of Lee and Pielke's β-equation:

$$\beta = \left[e(T_s) - e(T_a)\right] / \left[e_s(T_s) - e(T_a)\right] \tag{1.34}$$

$$\beta = \begin{cases} 0 & \theta \le \theta_m \\ \frac{1}{4}\left[1 - \cos(\pi(\theta - \theta_m)/(\theta_{fc} - \theta_m)\right]^2 & \theta_m < \theta \le \theta_{fc} \\ 1 & \theta > \theta_{fc} \end{cases} \tag{1.35}$$

where $e(T_s)$ is the surface vapor pressure; $e_s(T_s)$ is the saturated surface vapor pressure, $e(T_a)$ is the air vapor pressure; T_s is the surface temperature; T_a is the air temperature; θ is the volumetric soil moisture content; f_c is the field capacity of the topsoil layer; m is the moisture content correspondent to the monomolecular suction. The difference between equation (1.34) and the Lee and Pielke's β-equation is that θ_m terms are added here. θ_m should be considered because soil evaporation cannot continue when the soil suction becomes equal to or larger than the monomolecular suction.

② *Infiltration* Considering infiltration into a vertical uniform soil column when the surface is ponded, Green and Ampt proposed an infiltration model by assuming there is a wetting front that separates saturated soil above from soil below and by using Darcy's law. Compared with the other infiltration models, the Green-Ampt model has the advantages of simplicity, physically based characteristics, and measurable parameters. Mein and Larson (1973) extended it to model infiltration into uniform soil during a steady rain, and Moore and Eigel (1981) extended it to model infiltration into two-layered soil profiles during steady rains. Moreover, Jia and Tamai (1997) suggested a generalized Green–Ampt model for infiltration into multilayered soil profiles during unsteady rains. The generalized Green–Ampt model is summarized as follows.

Supposing that the wetting front is in the mth soil layer (see Figure 1.9), the infiltration rate can be expressed as equation (1.36):

$$f = k_m \left(1 + \frac{A_{m-1}}{B_{m-1} + F}\right) \tag{1.36}$$

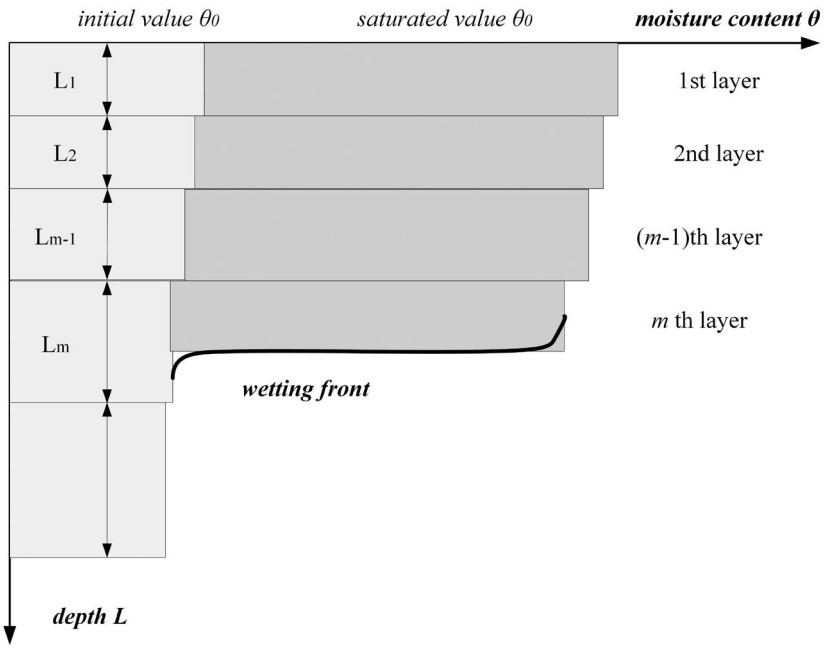

FIGURE 1.9 Schematic of infiltration into a multilayered soil profile.

where f is the infiltration rate; F is the accumulated infiltration, and the others are described later. The calculation of accumulated infiltration includes two cases. The accumulated infiltration is calculated in equation (1.37) if the surface ponding occurs with the wetting front at the (m–1)th layer and continues since then:

$$F - F_{m-1} = k_m(t - t_{m-1}) - A_{m-1} \cdot \ln\left(\frac{A_{m-1} + B_{m-1} + F}{A_{m-1} + B_{m-1} + F_{t_{m-1}}}\right) \tag{1.37}$$

Whereas it is calculated using equations (1.38)–(1.41), if the surface ponding begins at the present time step t_n with no ponding at the last time step t_{n-1}:

$$F - F_p = k_m(t - t_p) + A_{m-1} \cdot \ln\left(\frac{A_{m-1} + B_{m-1} + F}{A_{m-1} + B_{m-1} + F_p}\right) \tag{1.38}$$

$$F_p - F_{n-1} = I_p(t_p - t_{n-1});\ t_p = t_{n-1} + \frac{F_p - F_{n-1}}{I_p} \tag{1.39}$$

$$A_{m-1} = \left(\sum_{1}^{m-1} L_i - \sum_{1}^{m-1} L_i k_m / k_i + SW_m\right) \cdot \Delta\theta_m \tag{1.40}$$

$$B_{m-1} = \left(\sum_{1}^{m-1} L_i k_m / k_i\right) \cdot \Delta\theta_m - \sum_{1}^{m-1} L_i \Delta\theta_i;\ \ F_{m-1} = \sum_{1}^{m-1} L_i \Delta\theta_i \tag{1.41}$$

where SW is the capillary suction at the wetting front; k is the hydraulic conductivity in the wetted zone; θ_s is the moisture content in the wetted zone, θ_0 is the initial moisture content; t is the time; F_p is the accumulated infiltration at the instant of surface ponding; t_p is the time to surface ponding; I_p is the rain intensity during the nth time step when surface ponding occurs; t_{m-1} is the time when the wetting front reached the interface of mth and (m–1)th; L is the depth of wetting front; L_i is the thickness of the ith soil layer and $\Delta\theta = \theta_s - \theta_0$.

③ *Surface Runoff* In the WB group, surface runoff was estimated as precipitation minus evaporation. In the IA group, surface runoff can be obtained by doing a balance analysis of depression storage, precipitation, and evaporation on land surfaces. It is assumed that there is no infiltration in these two groups.

In the SV group, surface runoff consists of two parts, namely, infiltration excess (Horton-type runoff) during heavy rainfall periods and saturation excess (Dunne-type runoff) during the other periods. A heavy rainfall period is defined as a period during which the rainfall intensity is larger than the saturated soil hydraulic conductivity.

The infiltration excess $R1_{ie}$ was solved by applying the generalized Green-Ampt model to infiltration in three soil layers during heavy rainfall periods. The formulas to compute infiltration excess include equations (1.42) and (1.43):

$$\frac{\partial H_s}{\partial t} = P - E_0 - f - R1_{ie} \tag{1.42}$$

$$R1_{ie} = \begin{cases} 0 & H_s \le H_{s\max} \\ H_s - H_{s\max} & H_s > H_{s\max} \end{cases} \tag{1.43}$$

where H_s is the depression storage on the soil surface; $H_{s\max}$ is the maximum depression storage (set as 15 mm for paddy and 5 mm for other pervious land in this study); P is the rainfall; E_0 is the evaporation; f is the infiltration rate calculated with equation (1.36). In equation (1.43), the gradual variation of $R1_{ie}$ after $H_s > H_{s\max}$ is neglected because a time step of 1h is adopted in this study, which is believed to be long enough to justify the approximation. In addition, the interception storage of vegetation is assumed to be full; E_0 equals the potential evaporation, and transpiration is neglected during heavy rainfall periods.

The saturation excess $R1_{se}$ during the left periods may occur if the groundwater level in the unconfined aquifer rises and the topsoil layer becomes nearly saturated. It can be deduced by doing a balance analysis in every soil layer (the Richards model). The formulas include equations (1.44)–(1.52).

a. *Depression storage layer*

$$\frac{\partial H_s}{\partial t} = P(1 - Veg_1 - Veg_2) + Veg_1 \cdot R_{r1} + Veg_2 \cdot R_{r2} - E_0 - Q_0 - R1_{se} \tag{1.44}$$

$$R1_{se} = \begin{cases} 0 & H_s \le H_{s\max} \\ H_s - H_{s\max} & H_s > H_{s\max} \end{cases} \tag{1.45}$$

b. *Top soil layer*

$$\frac{\partial \theta_1}{\partial t} = \frac{1}{d_1}(Q_0 + QD_{12} - Q_1 - R2_1 - E_1 - Etr_{11} - Etr_{21}) \tag{1.46}$$

c. *Second soil layer*

$$\frac{\partial \theta_2}{\partial t} = \frac{1}{d_2}(Q_1 + QD_{23} - QD_{12} - Q_2 - R2_2 - Etr_{12} - Etr_{22}) \tag{1.47}$$

d. *Third soil layer*

$$\frac{\partial \theta_3}{\partial t} = \frac{1}{d_3}(Q_2 - QD_{23} - Q_3 - Etr_{13}) \tag{1.48}$$

$$Q_j = k_j(\theta_j)(j = 1,2,3) \tag{1.49}$$

$$\begin{aligned} &E_0 = \min\left\{E_p, (H_s + P_{in})E_p / (E_p + Q_p)\right\}; E_1 = E_s - E_0; \\ &P_{in} = P(1 - Veg_1 - Veg_2) + (Veg_1 R_{r1} + Veg_2 R_{r2}) \end{aligned} \tag{1.50}$$

$$\begin{aligned} &Q_0 = \min\left\{Q_p, (H_s + P_{in})Q_p / (E_p + Q_p)\right\}; Q_p = \min\left\{k_1(\theta_1), Q_{0\max}\right\}; \\ &Q_{0\max} = W_{1\max} - W_{10} - Q_1 \end{aligned} \tag{1.51}$$

$$\begin{aligned} &QD_{j,j+1} = k_{j,j+1} \cdot \frac{\psi_j(\theta_j) - \psi_{j+1}(\theta_{j+1})}{(d_j + d_{j+1})/2}; \\ &k_{j,j+1} = \frac{d_j \cdot k_j(\theta_j) + d_{j+1} \cdot k_{j+1}(\theta_{j+1})}{d_j + d_{j+1}} (j = 1,2) \end{aligned} \tag{1.52}$$

In the above equations, H_s is the depression storage on soil surface; H_{smax} is the maximum H_s; Veg_1 and Veg_2 are the fraction of tall and short vegetation, respectively; R_{r1} and R_{r2} are the drainage rate from tall and short vegetation, respectively; Q is the gravity drainage; $QD_{j,j+1}$ is the suction diffusion from the (j+1)th soil layer to the jth layer; E_0 and E_1 are the evaporation from the depression storage layer and top soil layer, respectively; Etr is the transpiration with the first subscript representing vegetation type (1 = tall vegetation and 2 = short vegetation) and the second one representing soil layer; R_2 is the subsurface runoff; θ is the moisture content; θ_s is the saturated moisture content; $k(\theta)$ is the hydraulic conductivity correspondent to θ; $\Psi(\theta)$ is the soil suction correspondent to θ; d is the thickness of the soil layer; $W = \theta \cdot d$ is the water storage of the soil layer, W_{10} is the initial water storage of

the top soil layer and the other notations are the same as mentioned above. Except where especially mentioned, the numbers or subscripts of all variables mean layer numbers with 0, 1, 2, and 3 representing the depression storage layer, top soil layer, second soil layer, and third soil layer, respectively.

The continuity of water movement was considered when the application of the generalized Green-Ampt model was switched into that of the Richards model and *vice versa*. When the application of the generalized Green-Ampt model is switched to that of the Richards model, the initial moisture contents of three unsaturated soil layers for the Richards model are computed based on the depth of the wetting front from the generalized Green-Ampt model. However, when the application of the Richards model is switched to that of the generalized Green-Ampt model, the moisture contents of the three soil layers from the Richards model provide initial values for the generalized Green-Ampt model, and no special treatment is required. It should be mentioned that there are some approximations in the application of the generalized Green-Ampt model. Though heat flux partition and surface temperature solution are also carried out, soil evaporation, canopy transpiration, and the redistribution of soil moisture below the wetting front are neglected. It is believed that these factors can be neglected during heavy rainfalls.

④ *Subsurface Runoff* The subsurface runoff was calculated using equation (1.53), according to the land slope and the soil hydraulic conductivity.

$$k_2 = k(\theta) \cdot \sin(slope) \cdot L \cdot d \tag{1.53}$$

where R_2 is the subsurface runoff from the unsaturated soil layers; L is the channel length in the contour belt, and others as denoted above.

Snow storage and melting processes were simulated using the temperature-index approach (Maidment, 1992) on a daily basis.

⑤ *Groundwater Flow and Groundwater Outflow* Taking account of the recharge from unsaturated soil layers and lifted groundwater as source terms, a quasi-3D simulation was performed for groundwater flow to consider the interactions between surface water and groundwater by using the Boussinesq equations (1.54)–(1.55).
unconfined aquifer:

$$C_u \frac{\partial h_u}{\partial t} = \frac{\partial}{\partial t}\left(k_u h_u \frac{\partial h_u}{\partial x}\right) + \frac{\partial}{\partial y}\left(k_u h_u \frac{\partial h_u}{\partial y}\right) + (Q_3 + WUL - RG - Per - E) \tag{1.54}$$

confined aquifers:

$$C\frac{\partial h}{\partial t} = \frac{\partial}{\partial t}\left(kD\frac{\partial h}{\partial x}\right) + \frac{\partial}{\partial y}\left(kD\frac{\partial h}{\partial y}\right) + (Per - GWP - Perc) \tag{1.55}$$

where C_u is the specific yield; C is the storage coefficient; h_u and h are the groundwater heads in the unconfined aquifer and confined aquifers, respectively; k_u and k are the

hydraulic conductivities of the unconfined aquifer and confined aquifers, respectively; D is the thickness of confined aquifers; Q_3 is the recharge from unsaturated soil layers; RG is the groundwater outflow to rivers; WUL is the water use leakage; GWP is the pumped groundwater; Per and $Perc$ are the percolation to the aquifer below; E is the evapotranspiration from groundwater when the unconfined groundwater level rises above the third soil layer. $E = F_{SV}Etr_{13}$ if h_u rises to the third soil layer; $E = F_{SV}\,(Etr_{12} + Etr_{13} + Etr_{22})$ if h_u rises to the second soil layer or $E = F_{SV}\,(E_s + Etr_{11} + Etr_{12} + Etr_{13} + Etr_{22})$ if h_u rises to the topsoil layer with the notations as described above.

Groundwater outflow was calculated by equation (1.56), according to the hydraulic conductivity k_b of riverbed material and the difference between river water stage H_r and groundwater level h_u.

$$RG = \begin{cases} k_b A_b (h_u - H_r)/d_b & h_u \geq H_r \\ -k_b A_b \left[1 + (H_r - Z_b)/d_b\right] & h_u < H_r \end{cases} \tag{1.56}$$

where A_b is the seepage area of the riverbed; Z_b is the elevation of the riverbed; d_b is the thickness of the riverbed material.

River flow. The river flow was routed for every sub-basin and a main channel by using the kinematic wave method, which can be expressed as equations (1.57) and (1.58).

$$\frac{\partial A}{\partial t} + \frac{\partial Q}{\partial x} = q_L \tag{1.57}$$

$$Q = \frac{A}{n} R^{2/3} S_0^{1/2} \tag{1.58}$$

where A is the area of lateral section; Q is the discharge; q_L is the lateral inflow of unit channel length; n is the Manning coefficient; R is the hydraulic radius; S_0 is the longitudinal slope of the river bed. In addition, $q_L = \Sigma[(R1 + R2 + RG + R_{sew} + Dx{\cdot}Dy]/L$, where Σ denotes summation of all contour belts in the sub-basin; R_{sew} is the sewerage in a contour belt of the sub-basin; Dx and Dy are the unit size in x and y directions; L is the channel length and the others as mentioned before.

⑥ *Anthropogenic Components* The water use in contour belt was deduced by using population and water use per capita. The water use per capita was decided according to statistics of water use in a river basin. In addition, water use leakage was deduced from water use and the leakage rate of the water supply system.

The sewerage was equal to water use subtracted by leakage. It was set as one part of the lateral inflow to the channel.

The groundwater lift has twofold utilization, the drinking water and the irrigation water. The drinking water was calculated according to the annual drinking water lift and the population distribution. The irrigation water was calculated based on the annual lift, paddy area, and irrigation period.

1.3.3 Concepts and Approaches for Dynamic Assessment of Water Resources

The scope of water resources assessed in the traditional approach includes surface water and groundwater, both of which exist in gravity-driven form. However, unsaturated soil moisture in vegetation root zones and intercepted precipitation on vegetation are effective for ecology, and evaporation from the depression layer of residential areas is also effective for people-living environment because it can wet the dry air and lower the air temperature in hot summer. Thus, these parts of evapotranspiration, i.e., the precipitation directly utilized by the ecosystem, should also be considered for water resources assessment. The traditional water resources can be called "special water resources", and those including the precipitation directly utilized by the ecosystem can be called "general water resources".

The general water resources comprise the sum of specialized water resources and the precipitation directly utilized by the ecosystem, which can be calculated as equation (1.59).

$$W = (R_s + R_g) + (E_i + E_d + E_t) \tag{1.59}$$

where the variables are defined as follows: W, general water resources; R_s, surface water resources; R_g, groundwater resources non-overlapped with surface water resources; E_i, interception of vegetation canopies; E_d, evaporation from depression layers of residential and vegetation areas; and E_t, vegetation transpiration, i.e., utilization of soil moisture non-overlapped with surface water and groundwater in vegetated areas. In addition, $R_s + R_g$ is the special water resources, and $E_i + E_d + E_t$ is the precipitation utilized by the ecosystem.

1.4 IMPLEMENTATION PROGRAMME OF THE CWAM

Based on determining the basic computation units and their topological relationships, there were 38 main computation modules in the model (Table 1.2). Modules 1–31 were the inherent computation modules of the WEP-L model. To realize the demand for refined simulation of different climatic and hydrological zones and geological and geomorphological units in large-scale regions, based on the design of the model architecture, modules 32–38 were developed to address the key issues such as spatial three-dimensional spreading of meteorological data, spatial differentiation of vegetation parameter assignments, and modification of the structure of the special air-sealed zones and their moisture movement parameters, etc. The overall computation process is shown in Figure 1.10.

1.4.1 Spatial and Temporal Spreading of Daily Meteorological Data over the Sub-Basins

First, according to the actual needs or existing results, the large-scale area will be divided into a number of subzones, such as administrative zones, climatic zones, water resource zones, etc., and as far as possible, the areas with drastic changes in topography will be separated from the flat areas. Then, based on the observed data of meteorological stations and the elevation where they are located in each subzone, a univariate regression relationship of meteorological data changes with elevation can be established zone by zone to obtain the coefficient of determination and the linear rate of change. If the coefficient of determination of the subzones is greater than 0.5, it is considered that the meteorological data in

TABLE 1.2 Main Module of the CWAM

Id	Name	Function
1	WEP_Main	Control structure framework of the main program.
2	Read_IO_File	Read input and output file names and convert them to absolute paths for file invocation.
3	Open_IO_File	Open the input and output files and prepare to read and write data.
4	Define_Para	Define parameters, variables, arrays, etc. (including time parameters).
5	Read_Para	Read data and parameters.
6	Set_Init_Status	Set initial and boundary conditions (flow, water table, etc.) for calculation units.
7	Landuse_Year	Land use was calculated year by year and reclassified into five categories.
8	River_alfa	Calculation of river-related roughness coefficients, such as Manning coefficient, and overbank effect parameters.
9	Sub_radi	Calculation of daily radiation in sub-basins.
10	P_Hour	Calculation of hourly rainfall based on daily rainfall downscaling.
11	Runoff_1_water	Calculation of the water and heat fluxes of water body in contour belts.
12	Runoff_2_soilveg	Calculation of the water and heat fluxes of soil and vegetation in contour belts.
13	Runoff_3_urban	Calculation of the water and heat fluxes of impervious area in contour belts.
14	Runoff_4_svir	Calculation of the water and heat fluxes of irrigated farmland in contour belts.
15	Runoff_5_svni	Calculation of the water and heat fluxes of non-irrigated farmland in contour belts.
16	Runoff_2_gampt	Calculation of the water and heat fluxes of soil and vegetation during heavy rainfall in contour belts using the Green-Ampt model.
17	Runoff_2_svei	Calculation of the water and heat fluxes of soil and vegetation during non-heavy rainfall in contour belts using the Richards model.
18	Accu_F	Calculation of the cumulative infiltration of soil and vegetation during heavy rainfall in contour belts using the Green–Ampt model.
19	Resis	Calculation of the aerodynamic resistance and canopy resistance.
20	Potential_ET	Calculation of the potential evaporation using the Penman equations.
21	Soil_E	Calculation of the evaporation from soils using the Penman equations.
22	Root_E	Calculation of the transpiration from soil layers by roots based on a root uptake model.
23	RFRM	Calculation of the surface temperature and the heat conduction into soil using the Force-Restore methods.
24	Unsaturated_K	Calculation of the unsaturated water conductivity corresponding to different soil water content using the Mualem equation.
25	Snow_ice	Calculation of the accumulation and melting of snow and ice.
26	Gwater	Calculation of the daily groundwater movement using the finite difference method.
27	Gw_River_exchange	Calculation of the exchange between groundwater and river runoff.
28	Conflux_Overland	Calculation of the confluence of overland flow using the one-dimensional motion wave method
29	Conflux_River	Calculation of the confluence of stream flow using the one-dimensional motion wave method.
30	Output_ViewRange	Output of the daily, monthly, and annual water cycle elements (water fluxes, resource quantities) in the concerned interval.
31	Output_Basin	Output of the daily, monthly, and annual water cycle elements (water fluxes, resource quantities) in the entire basin.
32	Sub_Mete_Zone	Distribution of daily meteorological data in the sub-basins.
33	Mon_Lai_Veg	Distribution of monthly vegetation data in the sub-basins.
34	Sub_Zone	Identification of the vadose zone structure type of the sub-basin.
35	Accu_Soil_Loess	Calculation of soil water movement in the Loess Plateau region
36	Accu_Soil_Karst	Calculation of soil water movement in the karst region
37	Accu_Soil_Frozen	Calculation of soil water movement in the cold region
38	Para_Soil_Air	Calculation of precipitation infiltration under the influence of air resistance.
39	ZoneCoef_Para	Partition setting of parameters to be debugged of the model.

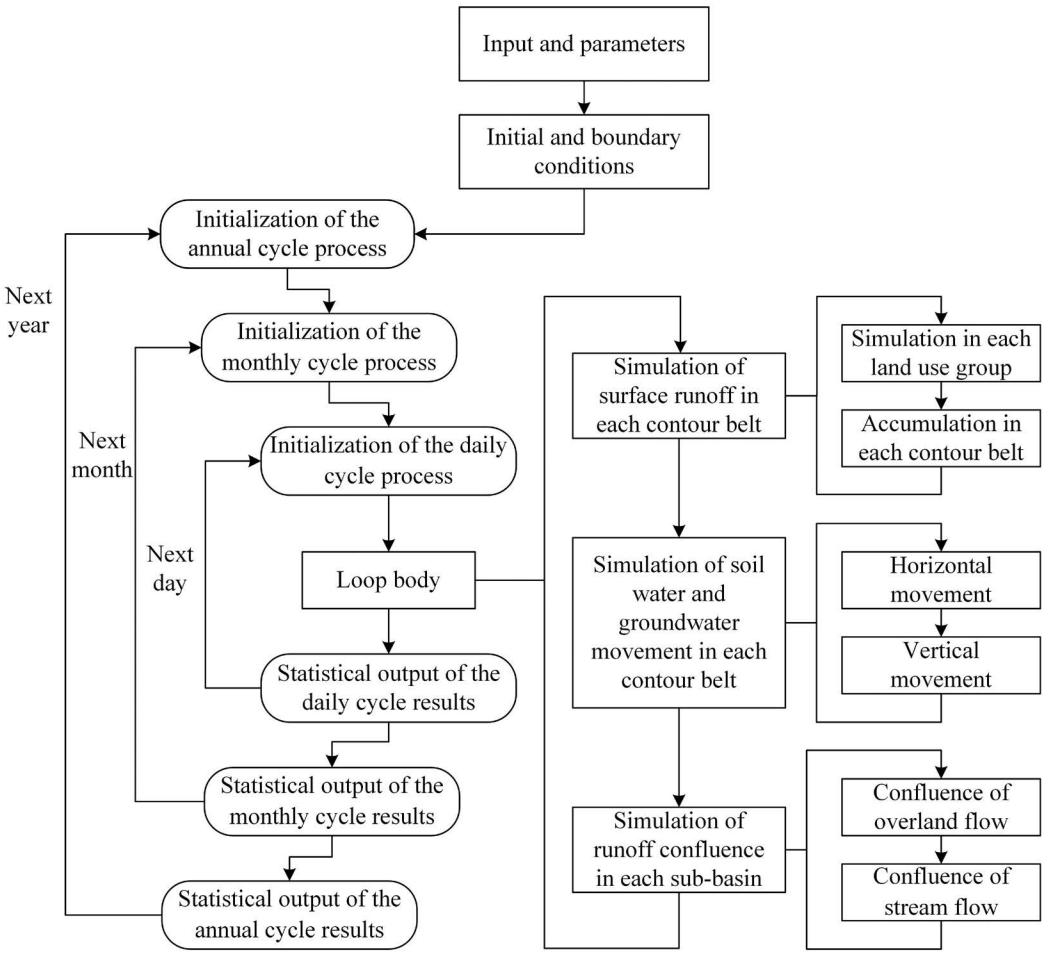

FIGURE 1.10 Calculation flowchart of the CWAM.

the region varies significantly linearly with elevation, and the spatial three-dimensional spreading method considering the influence of elevation is used to complete the interpolated spreading of the meteorological data on these subzones. Instead, a planar interpolation algorithm is used. Finally, the daily meteorological data are spread to all modeled sub-basins.

1.4.2 Zonal Calculation of Monthly Vegetation Data

Vegetation cover (*veg*) and leaf area index (*LAI*) are the two vegetation parameters that most significantly affect vegetation canopy interception, evapotranspiration, and transpiration and are characterized by seasonal and vertical zonal changes. First, the MODIS dataset of *LAI* and the *veg* data extracted from NDVI using the image meta-dichotomous model are used as data sources for the model LAI and veg. Furthermore, the large-scale area is divided into subzones, taking into account elevation changes. Finally, based on

the land use type data of each subzone, its 12-month LAI and veg are counted according to the classification of forests, grasslands, and crops to form a database of vegetation parameters.

1.4.3 Identification of the Structure Type of Vadose Zones in Each Sub-Basin

The study classified the structure types of vadose zones that may occur in China into four types: general soil bedrock type, loess swelling type, soil-epikarst type, and permafrost type. Therefore, the identification of the structure type of vadose zones to which the sub-basin belongs is the basis for correcting the water movement parameters of vadose zones. First, by analyzing and combining the profile of the study area to determine whether there is a wide range of special structures of vadose zones other than the soil bedrock type in the country. Then, the extent of the area with a particular vadose structure is determined with the help of the results of previous research or through methods such as cluster analysis. Finally, according to the position where the center of mass of sub-basin is located to determine the type of vadose structure it belongs to, set the parameter ID_Sub(*ix*) to identify it in order to call modules 35–37, where *ix* is the code of sub-basin. When ID_Sub is 0, 1, 2, and 3, it indicates that the vadose structural types of the sub-basin are general bedrock type, loess swelling type, soil-epikarst type, and permafrost type, respectively.

1.4.4 Improved Simulation of Soil Water Movement for Different Structures of Vadose Zones

On the one hand, the special structures of loess swelling type, soil-epikarst type, and permafrost type were analyzed in terms of the mechanism of their influence on soil water movement, and their corresponding mathematical simulation methods were proposed. For the loess swelling type area, the swelling soil deformation when absorbing water is mainly affected by the soil swelling pressure and self-weight stress. The soil swelling pressure varies with soil water content, and the self-weight stress varies with soil depth. This caused the decrease of porosity in the soil profile, which greatly affects the soil saturated moisture movement parameters and infiltration process. The soil-epikarst type area has a particular structure that includes soil, epikarst, and unsaturated zones. The uppermost soil layer is usually thin and sometimes even missing. Epikarst zone plays a key role in water storage and movement, as well as in transpiration of vegetation root systems, where the fissure network is strongly developed. The unsaturated zone has a poor fissure development, and its water capacity and permeability are significantly lower compared to those in the epikarst zone. For the permafrost-type area, the permafrost layer also acts as a barrier to water and affects the water cycle process. Furthermore, the changes in the depth of soil freezing and thawing play an important regulatory role in runoff in permafrost areas. Therefore, the study focused on quantitatively analyzing the variation of soil saturated water content and saturated hydraulic conductivity with soil depth in loess swelling type area, the role of epikarst zone on soil water storage and hydraulic conductivity in karst-developed areas, as well as the water and heat coupling process of permafrost in cold regions. The three parts are elaborated in detail by selecting typical basins in Chapters 3–5, respectively. On the other hand, the occurrence of air resistance in soils is common in rainfall conditions.

Based on the Green–Ampt model and the results of laboratory infiltration-runoff experiments, a modified Green–Ampt model was proposed to simulate infiltrations into layered soil profiles with the entrapped air under unsteady rainfall conditions, and introduced to the CWAM. Details are set out in Chapter 6.

1.4.5 Partition Settings for Model Parameters

Firstly, the large-scale region is divided into a number of parameter subzones based on climatic conditions, geological and geomorphological differences, and water distribution characteristics. Then, according to the type of vadose structure in each subzone, set the corresponding parameter type and its initial value. General parameters include maximum depression storage depth of land surface, soil saturated hydraulic conductivity, permeability of riverbed material, Manning coefficient, snow melting coefficient, and critical air temperature for snow melting. In addition, it is necessary to set several different parameters in special types of areas, such as loess swelling type, soil-epikarst type, and permafrost type.

REFERENCES

Abbott, M.B., Bathurst, J.C., Cunge, J.A. et al., 1986a. An introduction to the European hydrological system—Systeme Hydrologique Europeen, "SHE", 1: History and philosophy of a physically-based, distributed modelling system. Journal of hydrology, 87(1–2), 45–59.

Abbott, M.B., Bathurst, J.C., Cunge, J.A. et al., 1986b. An introduction to the European hydrological system—Systeme hydrologique European, "SHE", 2: Structure of a physically-based, distributed modelling system. Journal of hydrology, 87(1–2), 61–77.

Arnold, J.G. and Fohrer, N., 2005. SWAT2000: Current capabilities and research opportunities in applied watershed modelling[J]. Hydrological processes, 19(3), 563–572.

Avissar, R. and Pielke, R.A., 1989. A parameterization of heterogeneous land-surface for atmospheric numerical models and its impact on regional meteorology. Monthly weather review, 117, 2113–2136.

Brutsaert, W., 1982. Evaporation into the Atmosphere: Theory, History, and Applications. Kluwer academic, Dordrecht.

Calver, A., 1988. Calibration, sensitivity and validation of a physically-based rainfall-runoff model. Journal of hydrology, 103(1–2), 103–115.

Chen, R.S., Kang, E.S., Wu, L.Z. et al., 2005. Cold regions in China. Cold regions science and technology, 27(4), 469–475. (in Chinese).

Ciarapica, L. and Todini, E., 2002. TOPKAPI: A model for the representation of the rainfall-Runoff process at different scales. Hydrological processes, 16(2), 207–229.

Hartmann, A., Goldscheider, N., Wagener, T. et al., 2014. Karst water resources in a changing world: Review of hydrological modeling approaches. Reviews of geophysics, 52(3), 218–242.

Hewlett, J.D., 1982. Principles of Forest Hydrology. University of Georgia Press, Athens, GA.

Hu, Z. and Islam, S., 1995. Prediction of ground surface temperature and soil moisture content by the force-Restore method. Water resources research, 31(10), 2531–2539.

Jenson, S.K. and Domingue, J.O., 1988. Extracting topographic structure from digital elevation data for geographic information system analysis. Photogrammetric engineering and remote sensing, 54(11), 1593–1600.

Jia, Y., Kinouchi, T. and Yoshitani, J., 2005. Distributed hydrologic modeling in a partially urbanized agricultural watershed using WEP model. Journal of hydrologic engineering, 10(4), 253–263.

Jia, Y., Ni, G., Kawahara, Y. et al., 2001. Development of WEP model and its application to an urban watershed. Hydrological processes, 15(11), 2175–2194.

Jia, Y., Ni, G., Yoshitani, J. et al., 2002. Coupling simulation of water and energy budgets and analysis of urban development impact. Journal of hydrologic engineering, 7(4), 302–311.

Jia, Y. and Tamai, N., 1997. Modeling infiltration into a multi-layered soil during an unsteady rain. Journal of hydroscience and hydraulic engineering, 16(2), 1–10.

Jia, Y. and Tamai, N., 1998. Integrated analysis of water and heat balance in Tokyo metropolis with a distributed model. Journal of Japan society of hydrology and water resources, 11(1), 150–163.

Jia, Y., Wang, H., Zhou, Z. et al., 2006. Development of the WEP-L distributed hydrological model and dynamic assessment of water resources in the Yellow River basin. Journal of hydrology, 331(3–4), 606–629.

Kirkby, M.J. and Beven, K.J., 1979. A physically based, variable contributing area model of basin hydrology. Hydrological sciences journal, 24(1), 43–69.

Lee, T.J. and Pielke, R.A., 1992. Estimating the soil surface specific humidity. Journal of applied meteorology and climatology, 31, 480–484.

Li, X., Cheng, G.D. and Jin, H.J., 2008. Cryospheric change in China. Global and planetary change, 62, 210–218.

Liang, X., Lettenmaier, D.P., Wood, E.F. et al., 1994. A simple hydrologically based model of land surface water and energy fluxes for general circulation models. Journal of geophysical research: Atmospheres, 99(D7), 14415–14428.

Liu, H., Du, J., Jia, Y. et al., 2019. Improvement of watershed subdivision method for large scale regional distributed hydrology mode. Advanced engineering sciences, 51(1), 36–44. (in Chinese)

Maidment, D.R., 1992. Handbook of Hydrology. McGraw-Hill, New York.

Mein, R.G. and Larson, C.L., 1973. Modelling infiltration during a steady rain. Water resources research, 9(2), 384–394.

Monteith, J.L., 1973. Principles of Environmental Physics. Edward Arnold Publishers, London.

Moore, I.D. and Eigel, J.D., 1981. Infiltration into two-layered soil profiles. Transactions ASAE, 24, 1496–1503.

Noilhan, J. and Planton, S.A., 1989. Simple parameterization of land surface processes for meteorological models. Monthly weather review, 117, 536–549.

Perrin, J., Jeannin, P.Y. and Zwahlen, F., 2003. Epikarst storage in a karst aquifer: A conceptual model based on isotopic data, Milandre test site. Switzerland. Journal of hydrology, 279(1–4), 106–124.

Rui, X.F., 1996. Discussion of some problems on mechanism of runoff yield. Journal of hydraulic engineering, 9, 22–26. (in Chinese).

Sevruk, B., 1997. Regional dependency of precipitation-altitude relationship in the Swiss Alps. Climatic change, 36(3–4), 355–369.

Siriwardena, L., Finlayson, B.L. and Mcmahon, T.A., 2006. The impact of land use change on catchment hydrology in large catchments: The Comet River, Central Queensland, Australia. Journal of hydrology, 326(1–4), 199–214.

Su, N., 2010. Theory of infiltration: Infiltration into swelling soils in a material coordinate. Journal of hydrology, 395, 103–108.

Verdin, K.L. and Verdin, J.P., 1999. A topological system for delineation and codification of the Earth's river basins. Journal of hydrology, 218, 1–12.

Wagener, T., Wheater, H.S. and Gupta, H.V., 2004. Rainfall-Runoff Modelling in Gauged and Ungauged Catchments. Imperial College Press, London.

Wang, L., Wang, Z.J., Yin, H. et al., 2006. A distributed hydrological Model-GBHNM and its application in middle-scale catchment. Journal of glaciology and geocryology, 28(2), 256–261.

Wang, G.Q., Zhang, J.Y., He, R.M. et al., 2007. Trends of temperature change in middle of Yellow River and its impact to the evaporation potential. Journal of water resources and water engineering, 18(4), 32–36. (in Chinese).

Watanabe, K. and Osada, Y., 2017. Simultaneous measurement of unfrozen water content and hydraulic conductivity of partially frozen soil near 0 °C. Cold regions science and technology, 142, 79–84.

Xia, J., Wang, G.S., Tan, G. et al., 2004. Distributed time-variant gain hydrological model. Scientia sinica (Terrae), 34(11), 1062–1071.

Zhang, Z.C., Chen, X., Ghadouani, A. et al., 2011. Modeling hydrological processes influenced by soil, rock and vegetation in a small Karst basin of southwest China. Hydrological processes, 25(15), 2456–2470.

Zhang, Z.L., Fan, H.M., Guo, C.J. et al., 2008. Study on the relationship between flow velocity of sloping face and runoff characteristic under the simulated rainfall. Research of soil and water conservation, 15(6), 32–34. (in Chinese).